NASA/CR-1999-209330
ICASE Report No. 99-16

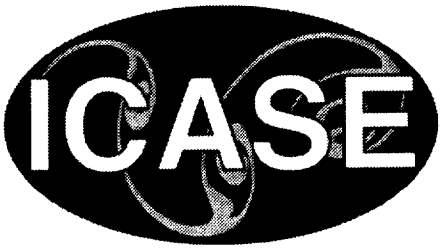

On the Stability of Three-dimensional Boundary Layers Part 1: Linear and Nonlinear Stability

Erik Janke
Old Dominion University, Norfolk, Virginia

Ponnampalam Balakumar
Old Dominion University, Norfolk, Virginia
and
ICASE, Hampton, Virginia

Institute for Computer Applications in Science and Engineering
NASA Langley Research Center
Hampton, VA

Operated by Universities Space Research Association

National Aeronautics and
Space Administration

Langley Research Center
Hampton, Virginia 23681-2199

Prepared for Langley Research Center
under Contract NAS1-97046

May 1999

Available from the following:

NASA Center for AeroSpace Information (CASI)
7121 Standard Drive
Hanover, MD 21076-1320
(301) 621-0390

National Technical Information Service (NTIS)
5285 Port Royal Road
Springfield, VA 22161-2171
(703) 487-4650

ON THE STABILITY OF THREE-DIMENSIONAL BOUNDARY LAYERS PART 1: LINEAR AND NONLINEAR STABILITY *

ERIK JANKE AND PONNAMPALAM BALAKUMAR

Abstract. The primary stability of incompressible three-dimensional boundary layers is investigated using the Parabolized Stability Equations (PSE). We compute the evolution of stationary and traveling disturbances in the linear and nonlinear region prior to transition. As model problems, we choose Swept Hiemenz Flow and the DLR Transition Experiment. The primary stability results for Swept Hiemenz Flow agree very well with computations by Malik et al. For the DLR Experiment, the mean flow profiles are obtained by solving the boundary layer equations for the measured pressure distribution. Both linear and nonlinear results show very good agreement with the experiment.

Key words. PSE, crossflow instability, 3D boundary layers

Subject classification. Fluid Dynamics

1. Introduction. The transition process without bypass in a three-dimensional boundary layer flow can be described by five main phases. *First*, in the receptivity phase, disturbances determined by the outer conditions (surface roughness, freestream turbulence, acoustic noise) are entering the boundary layer. In the region of their introduction, a wide spectrum of disturbances is present. Many of these initial disturbances decay, however, and only a few are amplified in the downstream flow. *Second*, the phase of exponential growth sees a slow amplitude growth of the few unstable modes. Due to its linearity, this phase can be well described by following the most unstable mode. *Third*, in the phase of nonlinear interaction, the disturbance amplitudes are large enough to interact nonlinearly, the uniform spanwise mean flow is modulated by the disturbances, and a disturbance saturation into an equilibrium stage can be observed. The location of the saturation onset, as well as the saturation amplitude level are strong functions of the initial conditions of disturbance amplitude, frequency and phase, which are determined by the receptivity mechanism. In this third phase, the mean flow profiles are being distorted, the well known co-rotating crossflow vortices are fully developed, and the boundary layer thickness varies strongly in spanwise direction. Due to the strong distortion of the boundary layer, inflectional mean flow profiles develop and we can distinguish a *fourth* phase, in which the boundary layer becomes unstable to three-dimensional high-frequency disturbances. The frequencies observed in this phase are an order-of-magnitude higher than the primarily unstable ones and this mechanism is usually referred to as secondary instability. Finally, an explosive growth of these high-frequency modes initiates the *fifth* phase, the breakdown to turbulence.

In the research of purely crossflow instability dominated incompressible boundary layers, significant progress was made within the last years. Pioneering experiments, in particular performed in Göttingen, Germany and in Tempe, Arizona, U.S.A., are accompanied by computational work that lives more and more up to the challenge of guiding the experiments. Using the Parabolized Stability Equations (PSE), Malik et al. [17] showed for Swept Hiemenz Flow that including traveling disturbances with a small amplitude in the analysis can significantly decrease the saturation amplitude and influence the onset of saturation in

*Old Dominion University, Department of Aerospace Engineering, Norfolk, VA 23529 (current emails: erik.janke@dlr.de, pbala@icase.edu). This research was supported by the National Aeronautics and Space Administration under NASA Contract No. NAS1-97046 while the authors were in residence at the Institute for Computer Applications in Science and Engineering (ICASE), NASA Langley Research Center, Hampton, VA 23681-2199.

comparison with a purely stationary computation. Incorporating the receptivity to surface roughness in his PSE computations for the DLR Transition Experiment and also introducing initially small amplitude traveling modes, Bertolotti [4] arrived at results that are in excellent agreement with the measurements. Joslin and Streett [13] showed for stationary crossflow vortices that prior to the nonlinear interaction of the disturbances, linear superposition of the smaller amplitude modes can explain wave angle and phase adjustments observed in experiments by Arnal and Juillen [1]. Also, results by Kohama et al. [14] and Reibert et al. [18] for a swept wing boundary layer in very benign environmental conditions showed the existence of a high-frequency secondary instability that is caused by the inflectional deformation of the mean flow profiles.

In the present paper, we study the linear, nonlinear and secondary stability of the Swept Hiemenz Flow model problem and of the crossflow dominated boundary layer flow in the DLR Transition Experiment. For the sake of a more systematic presentation of the results, we divide the paper in two parts. Starting from a mean flow computation and a nonlinear stability analysis, we obtain the equilibrium solutions for each problem using the PSE in Part 1. In Section two of Part 1, we describe the present formulation for the mean flow computation and the primary stability analysis using the PSE. Sections three and four contain results from linear and nonlinear PSE computations for Swept Hiemenz Flow and the DLR Transition Experiment, respectively. We then determine the local stability characteristics in the equilibrium region using temporal Floquet analysis in Part 2 of this paper. There, the main focus is on investigating the existence of multiple roots in the eigenvalue spectrum of the modified mean flow in the region of nonlinear disturbance saturation.

2. Formulation. In this section, we present the mean flow computation and describe the PSE formulation. Figure 2.1 shows the coordinate systems that we use in the computations. The coordinates (x_1, x_2, x_3) represent the body-fixed coordinate system, and the $(\bar{x}_1, \bar{x}_2, \bar{x}_3)$ coordinates stand for the vortex-oriented system which is applied in the secondary stability analysis.

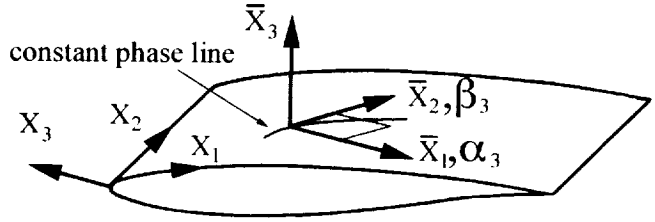

FIG. 2.1. *Body-fixed (x_1, x_2, x_3) and Galilean coordinate system $(\bar{x}_1, \bar{x}_2, \bar{x}_3)$*

2.1. Basic Flow. For a general quasi-three dimensional geometry and a corresponding coordinate system (Figure 2.1), we define a steady incompressible basic flow $Q_0\ (x_1, x_2, x_3) = \{U_0, W_0, V_0, P_0\}^T$. Assuming no variations of the basic flow in the spanwise direction, introducing a stream function Φ (Equation 2.1), and defining the mean flow components according to Equation 2.2:

$$\Phi = \sqrt{\nu^* x_1^* U_e^*} f(x_1^*, \eta)\ ;\ \eta = \frac{x_3^*}{\sqrt{\nu^* x_1^* / U_e^*}}\ ;\ m = \frac{x^*}{U_e^*} \cdot \frac{dU_e^*}{dx_1^*}\ , \tag{2.1}$$

$$U_0^* = \partial\Phi/\partial x_3^*\ ;\ V_0^* = -\partial\Phi/\partial x_1^*\ ;\ W_0^* = W_\infty^* \cdot g(x_1^*, \eta)\ , \tag{2.2}$$

we can write the boundary layer equations and the boundary conditions for a quasi-three-dimensional flow in the following form, where primes denote differentiation with respect to η :

$$f''' + \frac{m+1}{2} f \cdot f'' + m \cdot (1 - f'^2) = x_1 \cdot (f' \cdot \frac{\partial f'}{\partial x_1} - f'' \cdot \frac{\partial f}{\partial x_1}) ,$$

$$g'' + \frac{m+1}{2} f \cdot g' = x_1 \cdot (f' \cdot \frac{\partial g}{\partial x_1} - g' \cdot \frac{\partial f}{\partial x_1}) , \tag{2.3}$$

$$f = f' = g = 0 \quad at \quad \eta = 0 \quad ; \quad f' = g = 1 \quad at \quad \eta \to \infty .$$

Here, U_e^* is the inviscid velocity in the chordwise direction, W_∞^* is the constant inviscid velocity in the spanwise direction, and m is the similarity parameter. This set of equations is solved using the two-point, fourth-order-accurate compact scheme ([16]) in the wall normal direction and a second-order-accurate three point upwind scheme in the streamwise direction.

2.2. Parabolized Stability Equations. In the Parabolized Stability Equations approach, one attempts to construct an approximate solution of the Navier-Stokes Equations. The concept was introduced by Herbert and Bertolotti [10] and applied to linear and nonlinear Blasius boundary layer flow by Bertolotti et al. [3]. Now, it has been well developed and applied to two- and three-dimensional incompressible and compressible boundary layer flows [6, 2, 17].

If we write the total flow quantity $Q=\{V,P\}^T=\{U, W, V, P\}^T$ as the summation of the mean flow $Q_0=\{V_0,P_0\}^T=\{U_0, W_0, V_0, P_0\}^T$ and the disturbance $q_1=\{v_1,p_1\}^T=\{u_1, w_1, v_1, p_1\}^T$, the Navier-Stokes equations for the disturbances quantities become :

$$\nabla \cdot v_1 = 0 , \tag{2.4}$$

$$\frac{\partial v_1}{\partial t} + (v_1 \cdot \nabla)v_1 + (V_0 \cdot \nabla)v_1 + (v_1 \cdot \nabla)V_0 = - \nabla p_1 + \frac{1}{Re}\nabla^2 v_1 . \tag{2.5}$$

The central idea of the PSE formulation is to split the disturbance quantities into a slowly varying shape function and an oscillatory wave part as:

$$q_1(x_1, x_2, x_3, t) = \sum_{n=-\infty}^{\infty} \sum_{m=-\infty}^{\infty} \hat{q}_{1,mn}(x_1, x_3) e^{i \int \alpha_{1,mn} dx_1 + im\beta_1 x_2 - in\omega t} , \tag{2.6}$$

where β_1 is the spanwise wave number, ω is the frequency, α_1 is the wave number in the streamwise direction, and $\hat{q}_{1,mn}$ is the vector of the shape functions. The indices m and n are the Fourier summation indices and also denote the mode number (m,n). Substituting this into Equations 2.4, 2.5 and neglecting the second derivative of the shape function in the x_1-direction, we obtain the PSE (Equation 2.7) for each Fourier component. In Equation 2.7, the vector S_{mn} represents the Fourier component of the nonlinear term $(v_1 \cdot \nabla)v_1$, and A, B, C, D, E are (4×4) coefficient matrices.

$$A_{mn}\frac{\partial^2 \hat{q}_{1,mn}}{\partial x_3^2} + B_{mn}\frac{\partial \hat{q}_{1,mn}}{\partial x_3} + C_{mn}\hat{q}_{1,mn} = D_{mn}\frac{\partial \hat{q}_{1,mn}}{\partial x_1} + E_{mn}\frac{\partial^2 \hat{q}_{1,mn}}{\partial x_1 \partial x_3} + S_{mn} \tag{2.7}$$

We note that the linear PSE are obtained by setting the indices m and n in Equation 2.7 to one, and by dropping the nonlinear term S_{mn}. Further, assuming that the amplitude part $\hat{q}_1$ of the disturbance quantity

is no longer a function of the streamwise location, but depends only on the normal coordinate, the two remaining terms on the right hand side of Equation 2.7 vanish and we obtain the linear stability equation.

In the spatial framework of the PSE, we have the unknown wave numbers α_1, β_1, and the frequency ω in addition to the unknown shape functions $\hat{q}_1$. Fixing the real frequency ω and the real spanwise wave number β_1, a relation to determine the complex streamwise wave number α_1 is still missing. This forms the main difficulty in the PSE formulation, since both the shape functions and the phase of the disturbance quantities depend on the streamwise coordinate (Equation 2.6). In a non-parallel mean flow, the different physical quantities grow at different rates, and thus, one can determine the growth rate $\sigma_1 = -\alpha_{1,imag}$ only from the computed wave number α_1 based on some quantity (e.g., velocities, pressure, or energy). Usually, the wave number α_1 is computed at the location in the boundary layer where the disturbance quantities become maximal. This location slowly varies in the marching direction. The procedure to compute α_1 at a streamwise station is described as follows. Starting with an initial guess that is found by solving the linear eigenvalue problem at $x_1 = x_0$, one marches to the next station $x_1 = x_0 + \Delta x_1$ and solves for the shape functions $\hat{q}_1$ assuming that $\alpha_1(x_1 = x_0 + \Delta x_1) = \alpha_1(x_0)$. Approximating the change in the shape functions with a Taylor Series at $x_1 = x_0 + \Delta x$, one can derive Equation 2.8 to update α_1 at $x_1 = x_0 + \Delta x_1$ as :

$$\alpha_{1,new} = \alpha_{1,old} + \frac{1}{i \cdot \hat{q}_1} \left(\frac{\partial \hat{q}_1}{\partial x_1} \right)_{x_3 = x_3(\hat{q}_{1,max})} , \tag{2.8}$$

where $\hat{q}_1$ stands for any physical quantity in the flow field. Updating the shape functions and iterating until the change in α_1 is less than a defined tolerance, the solution at this station is obtained and the procedure repeated at the next streamwise station. The PSE method is very efficient, since it takes only a few iterations on α_1 to obtain an accurate solution, provided that the gradients in the flowfield are moderate. In our formulation, the PSE are solved by introducing a new vector of unknowns $\bar{q}_1 = \{\hat{u}_1, \partial\hat{u}_1/\partial x_3, \hat{u}_2, \partial\hat{u}_2/\partial x_3, \hat{u}_3, \hat{p}_1\}^T$ that allows for a discretization of the wall-normal direction using the two-point, fourth-order-accurate compact scheme [16]. For the derivatives in the streamwise direction, we employ a first-order-accurate two-point upwind scheme.

3. Swept Hiemenz Flow.

3.1. The Basic Flow. The model problem of Swept Hiemenz Flow represents an exact solution to the Navier-Stokes Equations and can be used to model the leading edge region of a swept wing. The inviscid velocity distributions are given by:

$$U^* = c \cdot x_1^* \;\; ; \;\; V^* = -c \cdot x_3^* ; \;\; W^* = W_\infty^* = const. \;\; . \tag{3.1}$$

Further, we define the nondimensional frequency F, the constant local length scale l^*, and the stream- and spanwise Reynolds numbers Re and $\bar{Re}$, respectively, in Equation 3.2. The mean flow profiles can be obtained

$$F = 2\pi\nu^* f^*/(W_\infty^*)^2 \;\; ; \;\; l^* = \sqrt{\nu^*/c} \;\; ; \;\; Re = \frac{U_\infty^* \cdot l^*}{\nu^*} \;\; ; \;\; \bar{Re} = \frac{W_\infty^* \cdot l^*}{\nu^*} \tag{3.2}$$

by solving the Falkner-Skan-Cooke equations ([15, 17]), which are the homogeneous version of Equations 2.3 with m=1. The results are obtained for $\bar{Re}$=500, F= $0.75 \cdot 10^{-4}$ and a spanwise wave number of β_1=0.4. The chosen value for F is close to the most amplified frequency for this flow.

3.2. Nonlinear Analysis. Following the previous work by Malik et al. [17], we investigate the evolution of stationary and traveling disturbances with and without wave interaction. In particular, we consider the interaction of a stationary and a traveling disturbance of similar initial amplitude, as well as the interaction of a stationary disturbance with larger amplitude and a traveling disturbance with smaller amplitude. Figure 3.1

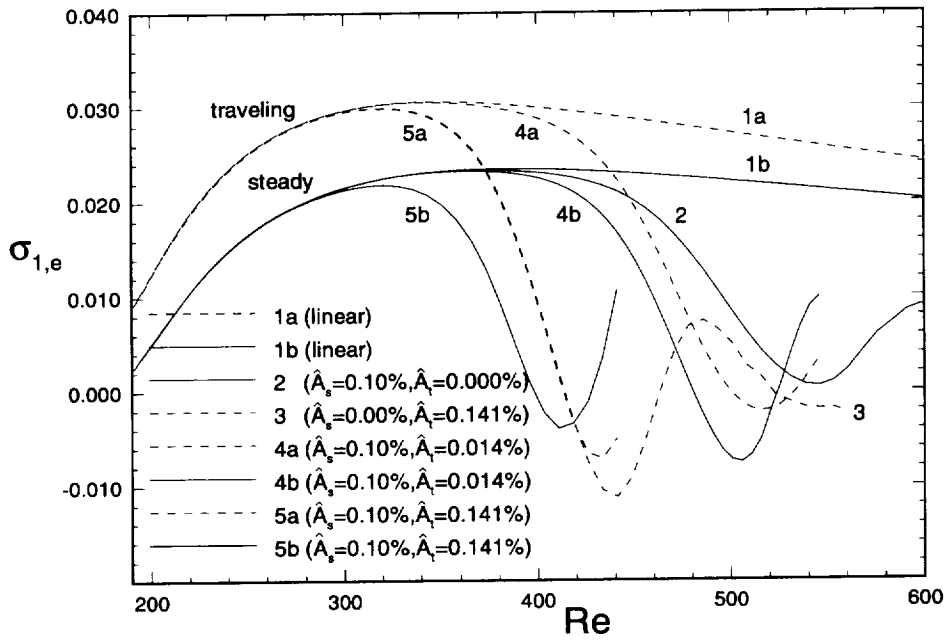

FIG. 3.1. *Growth rates based on disturbance-energy*

shows the growth rates for different initial amplitude levels $\hat{A}$. The *rms*-amplitude $\hat{A}$ is defined by $\hat{A} = \sqrt{(u_1^2 + w_1^2)_{max}}/\,W_\infty$, and the computed initial disturbances are introduced at Re=186. The computations are performed including eight modes in the spanwise and frequency domain and the results agree with the results by Malik et al. [17]. It can be seen from Figure 3.1 that the interaction of a larger amplitude stationary with a smaller traveling disturbance leads to an earlier saturation of the stationary disturbance. On the other hand, the nonlinear evolution of the traveling disturbance is not affected by the stationary vortex when both initial modes are of similar amplitude.

The influence of including a small amplitude traveling disturbance in the computations is presented in Figures 3.2 and 3.3, where we show the evolution of the stationary and traveling disturbance amplitudes. In Figure 3.2, we plot the results for the purely steady case, and in Figure 3.3 for a case where a small amplitude traveling disturbance interacts with the stationary vortex. The latter case will be referred to as the "lower-frequency" case from now on. For the purely stationary case, we observe that both the u_1- and w_1-components are fully saturated at $Re \simeq 550$, and that the saturation amplitude levels are $\hat{A}_s \simeq 24\%$ for the u_1-component and $\hat{A}_s \simeq 17\%$ for the w_1-component. For the "lower-frequency" case with a primary frequency of F=0.75·10^{-4}, we see that the stationary disturbances saturate at $Re \simeq 480$ and the amplitude levels are $\hat{A}_s \simeq 10\%$ and $\hat{A}_s \simeq 8\%$ for the u_1 and w_1-component, respectively. Also, since the traveling disturbances grow longer in that case (see curve 4a in Figure 3.1), they reach larger amplitude levels than the stationary disturbances.

Next, we document various velocity profiles for the purely stationary case. At the streamwise location where the stationary disturbances are saturated (Re=546), we plot the shapes of the individual Fourier modes for the velocity components along the stationary vortex (w_1), and perpendicular to it (u_1) in the Galilean coordinate system ($\bar{x}_1, \bar{x}_2, \bar{x}_3$) in Figure 3.4. Obviously, the first seven modes of the component

along the vortex contain important information, and thus, it is advisable to include at least eight modes in the computation. We also observe that the fundamental mode β_1 along the stationary vortex is very large at this Reynolds number ($\hat{A} \simeq 30\%$) and shows the typical structure observed in the experiments just before the secondary instability mechanism causes transition.

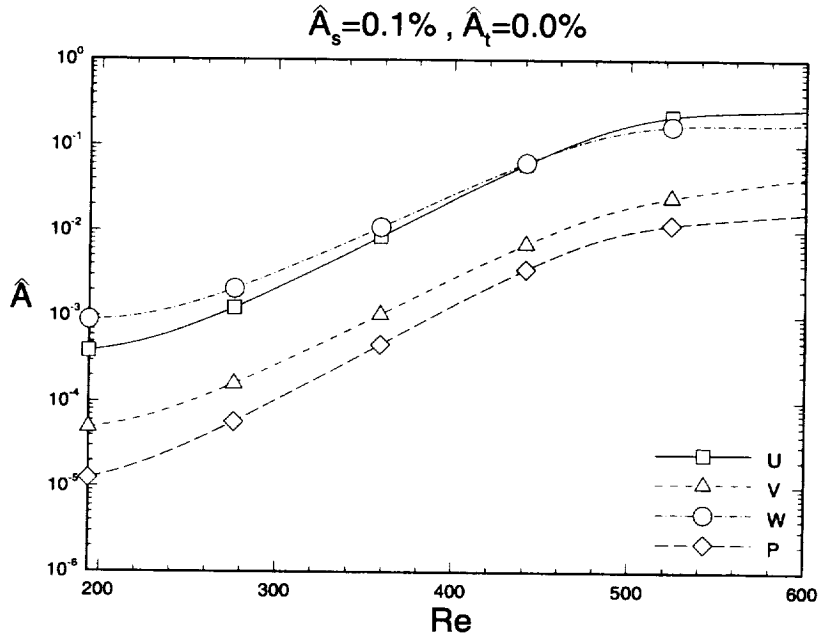

FIG. 3.2. *Amplitudes of the primary disturbances for the purely stationary case*

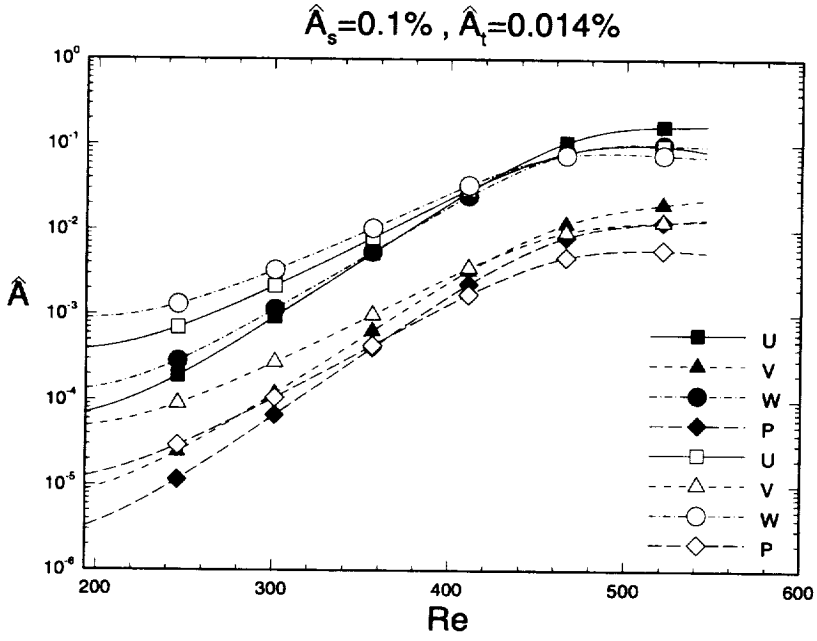

FIG. 3.3. *Primary disturbance amplitudes for the "lower-frequency case" (solid : traveling mode; hollow : steady mode)*

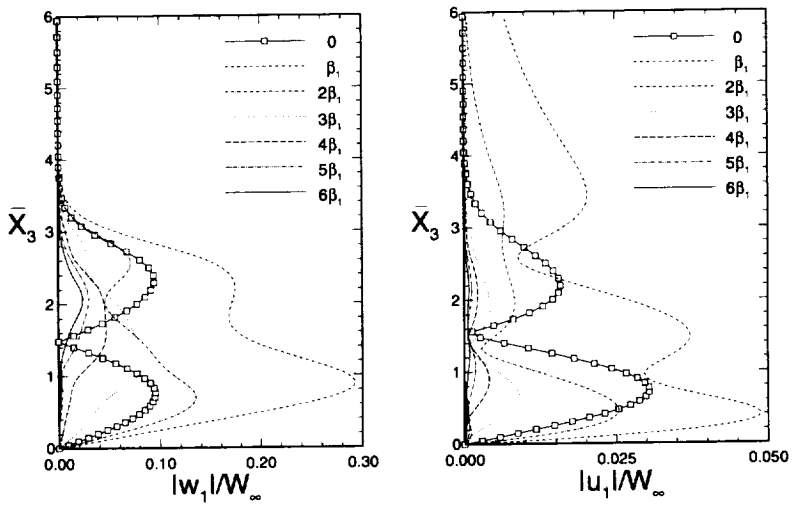

FIG. 3.4. *Shape functions of individual modes at* Re=546

Figure 3.5 shows the total velocity component tangential to the stationary vortex W_2 in the $\bar{x}_1, \bar{x}_3$-plane at four different locations within one wavelength perpendicular to the vortex. Finally, in Figures 3.6a)-d), we show the total velocity components (mean flow and disturbance) along the stationary vortex (W_2) and in the wall-normal direction (V_2) at two streamwise positions and at different normal locations. At Re=486, a developed peak-valley structure of the W_2-component is observed, and spanwise gradients in the normal velocity component are seen as well. At Re=546, however, an intricate spanwise variation of both plotted velocity components is noted. The increased inflectional character of the spanwise velocity profiles corresponds to the growing instability of the flow. Further, the strong spanwise gradients in the wall-normal velocity component (see Figure 3.6(d)) indicate the presence of a strong localized fluid-exchange mechanism between the wall region and the outer flow. As in Figure 3.5, the inflectional character of the profiles is clearly observed. These strongly inflectional profiles in all coordinate directions are the origin of the secondary instability that will be studied in Part 2 of this paper.

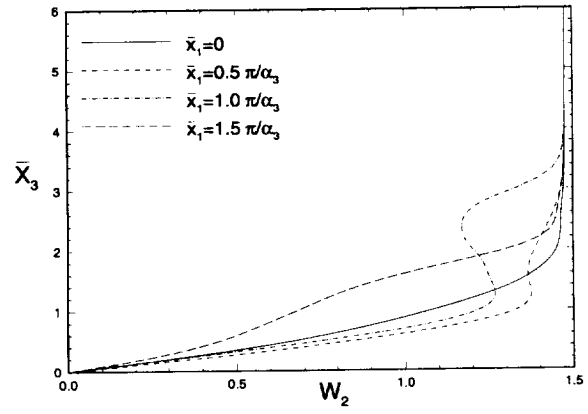

FIG. 3.5. *Total flow quantity at different spanwise stations for* Re=546

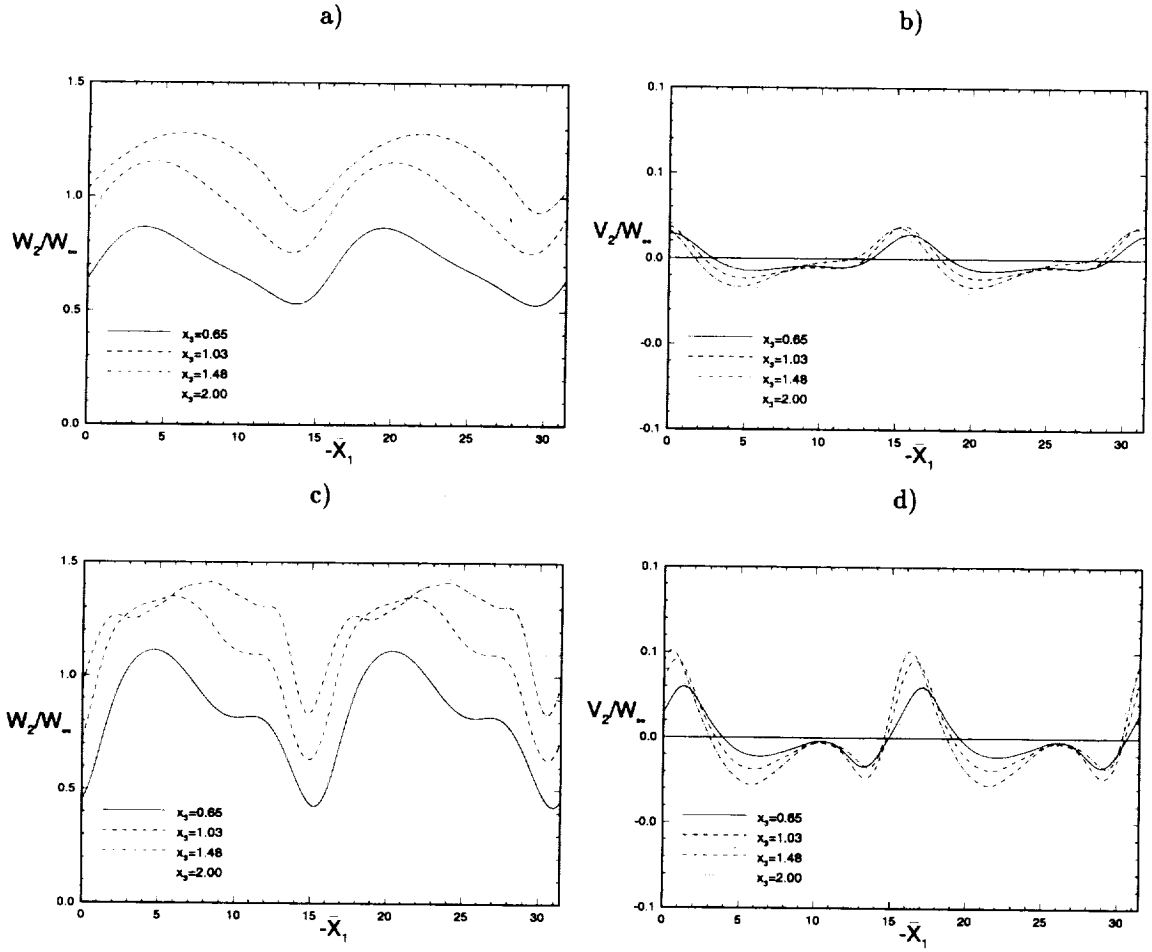

FIG. 3.6. *Horizontal cuts of the modified mean flow at two streamwise locations (a), b) at Re=486; c), d) at Re=546)*

4. DLR Transition Experiment. In this section, we investigate the linear and nonlinear evolution of stationary and traveling disturbances for the experiment reported by Deyhle and Bippes [9]. The experimental pressure gradient across the entire swept flat plate is favorable, and hence, the transition in the boundary layer is dominated by a purely crossflow type instability. Because of the wide variety of the investigated parameters and the well documented experimental data, this transition experiment is of high value for a numerical investigation of the crossflow instability mechanisms.

4.1. The Basic Flow. The experiment was performed for a freestream velocity of Q^*_∞=19 m/s, a sweep angle of ϕ=45°, and a chord length of the model of c^*=0.5m. In order to compensate for blockage effects and problems with the simulation of infinite swept wing conditions using end plates, Deyhle and Bippes [9] suggest the use of Q^*_∞=20.5 m/s and ϕ=43.5° instead. Our computations are done for the latter parameters and a Reynolds number based on the chord length of Re_∞=683,000, where $Re_\infty = Q^*_\infty \cdot c^*/\nu^*$. Further, we use $U^*_{e,0}$ and $l^*_0=(\nu^* \cdot x^*_{1,0}/U^*_{e,0})^{1/2}$ as the velocity scale and length scale, respectively, where $x^*_{1,0}$ and $U^*_{e,0}$ are the streamwise coordinate and the freestream velocity in the x_1-direction at the location where we introduced the disturbances. The turbulence level during the experiment is specified as Tu=0.15%. Even though this value represents a fairly benign environment, it is still high in comparison to the turbulence level present in the experiments performed by Reibert et al. [18] and Saric et al. [19] where they quote a

value of Tu=0.04% at a speed of Q^*_∞=20 m/s ([7]). In the DLR Experiment, traveling modes are present in the flow and one needs to consider these in the computations when comparing with the experimental results. Further, the fact of the initial presence of traveling modes complicates the isolation of the physical mechanisms considerably.

In contrast to previous work which used a Falkner-Skan-Cooke (FSC) similarity solution to fit the measured data, we compute the mean flow profiles directly from the measured outer velocity distribution that was obtained by courtesy of the DLR (Bertolotti [5]) and is given in Figure 4.1. In Figure 4.2, we compare the boundary layer profiles along the inviscid streamline U_t and the crossflow velocity profiles U_c resulting from the present approach and the FSC solution (Deyhle and Bippes [9]) with the experiment. We note a good agreement of the computed with the measured profiles.

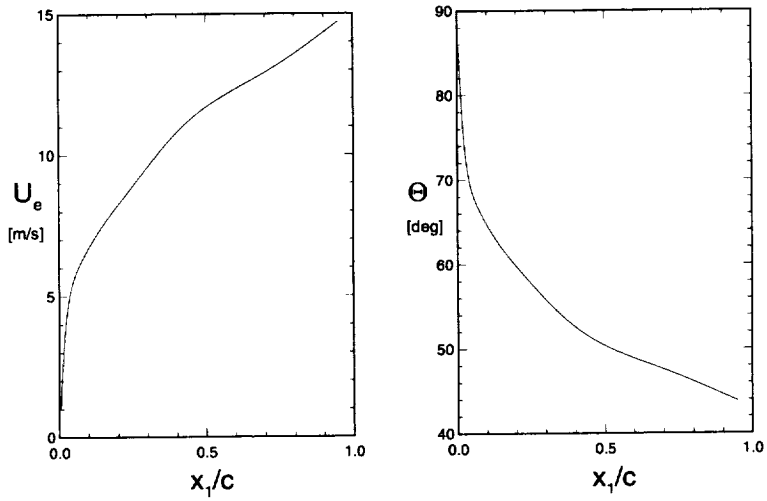

FIG. 4.1. *Measured outer velocity distribution and angle of inviscid streamline*

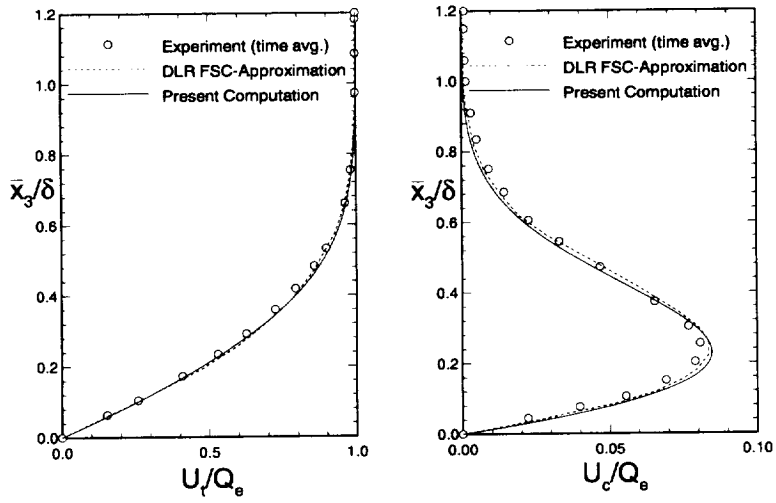

FIG. 4.2. *Mean flow profiles tangential and perpendicular to the streamline at* x_1/c=0.4

4.2. Linear Stability Analysis. First, we conduct a local stability analysis of the undisturbed mean flow. In the spatial formulation of the local stability analysis, we consider a normal mode of the form :

$$q_1(x_1, x_2, x_3, t) = \hat{q}_1(x_3) e^{i\alpha_1 x_1 + i\beta_1 x_2 - i\omega t} , \tag{4.1}$$

where α_1 is the complex wave number in the chordwise direction, β_1 is the real wave number in the spanwise direction, and ω is the real frequency. The wave vector k_{real}, the wavelength λ and the wave angle Ψ_1 are defined in Equation 4.2.

$$k_{real} = \{\alpha_{1,real}, \beta_1\}^T \; ; \; \lambda = \frac{2\pi}{\sqrt{\alpha_{1,real}^2 + \beta_1^2}} = \frac{2\pi}{|k_{real}|} \; ; \; \Psi_1 = tan^{-1} \frac{\beta_1}{\alpha_{1,real}} \tag{4.2}$$

According to Mack (1984), two families of most unstable modes are present in three-dimensional boundary layers. Figure 4.3 depicts the propagation direction of the two unstable families. It also defines Ψ as the angle between the wave vector k_{real} and the inviscid streamline.

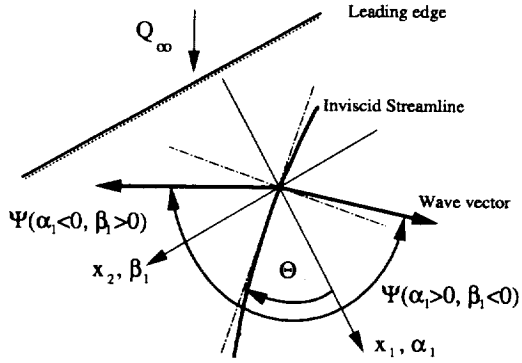

FIG. 4.3. *Definition of the wave angle Ψ and the angle of the inviscid streamline Θ*

In order to compare our linear results with experimental data, we consider the experiment performed by Deyhle et al. [8]. First, we show two unstable disturbance families for the arbitrary frequency of f^*=150 Hz versus the wavelength in the spanwise direction $\lambda^*_{z_2}$. From Figure 4.4, it is seen that the more unstable disturbances ($\beta_1 > 0$) propagate in the direction of the centrifugal force induced by the inviscid streamline.

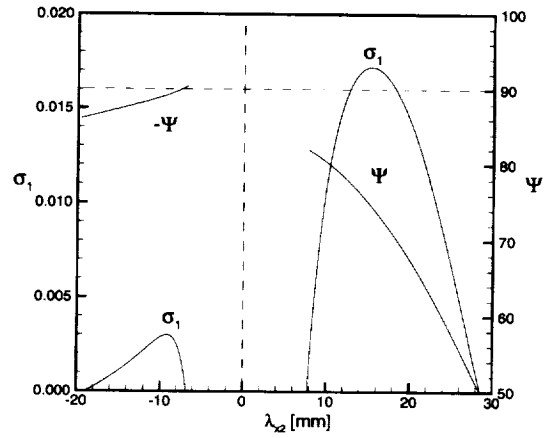

FIG. 4.4. *Two unstable disturbance families (x_1/c=0.7, f^*=150 Hz)*

Second, we compute wavelength, wave angle and phase speed at a streamwise location of x_1/c=0.7 as functions of the frequency by solving the spatial eigenvalue problem. Considering the temporal eigenvalue problem, the group velocity was determined. In Figures 4.5 and 4.6, we plot the wave angle Ψ relative to the angle of the inviscid streamline, the wavelength $\lambda = 2\pi/|k_{real}|$, the phase speed $C_{phase} = \omega/|k_{real}|$ and the group velocity $C_{group} = |\partial\omega/\partial k_{real}|$ for both families. The results are presented for the most unstable wave at a fixed frequency. Between the two modes with positive and negative β_1, the mode with a positive spanwise wave number has the largest growth rate. It is this family with a positive β_1 that seems to match the experimental results reasonably well. Considering the results for the wave angle, the wave length and the phase velocity, we note a better agreement with the experiment than for the group velocity results. However, Deyhle et al. [8] report experimental uncertainties in determining the group velocity, which might also account for the deviations in these results.

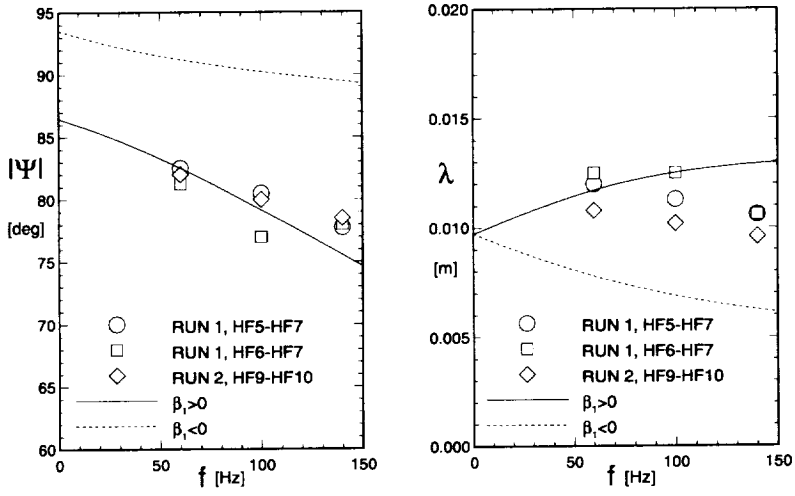

FIG. 4.5. *Experimental results and local theory at x_1/c=0.7*

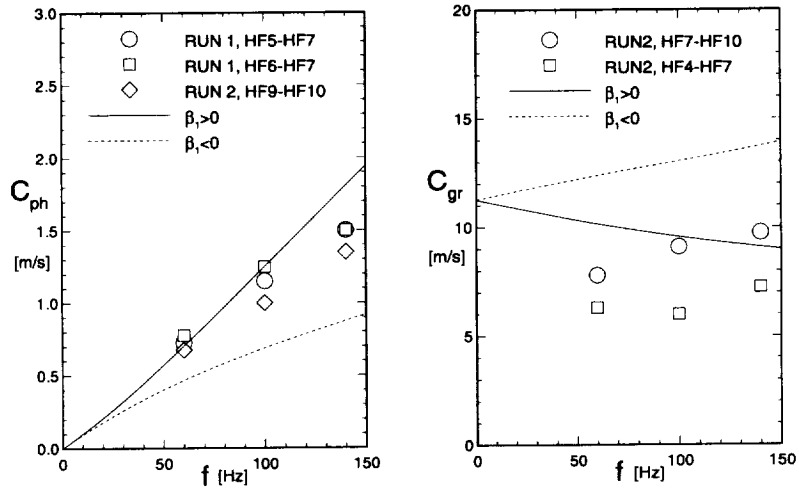

FIG. 4.6. *Experimental results and local theory at x_1/c=0.7*

Next, and reconsidering the experiment described in Section 4.1, we show the results of a local stability analysis performed at different streamwise locations. Thereby, the critical points and the locally most amplified steady and traveling disturbances are determined.

In Figure 4.7, the nondimensional growth rates σ_1 for stationary disturbances are plotted versus the spanwise wave number β_1 at different chordwise positions. It can be seen that the local theory predicts an increase of the unstable spanwise wave number range in the downstream direction for the stationary disturbances. The critical point for the stationary disturbances is found at x_1/c=0.067 for β_1=0.174 ($\lambda^*_{z_1}$=10.5mm). The locally most amplified wave number is determined as β_1=0.295 at x_1/c=0.40, where the chordwise wave number is α_1=(-0.33509,-0.01401). Table 1 contains the locally most amplified spanwise wave numbers, as well as the corresponding growth rates, dimensional spanwise wavelengths and wave angles.

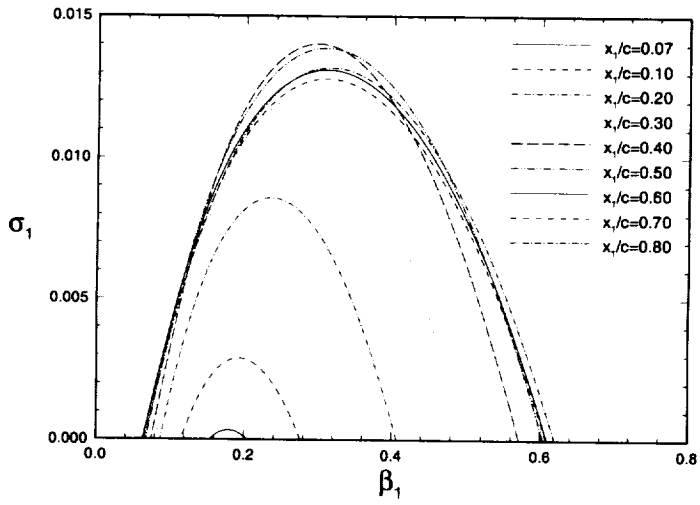

FIG. 4.7. *Stationary growth rates from a local analysis*

Table 1: Locally most amplified eigenpairs at different chordwise locations (f^*=0 Hz)

x_1/c	$\sigma_1 = max.$	$\lambda_{z_1,\sigma_1=max}[mm]$	$\beta_{1,\sigma_1=max.}$	$\Psi_{\sigma_1=max.}$
0.07	0.00033	10.43	0.177	87.60°
0.10	0.00289	10.92	0.193	87.45°
0.20	0.00858	11.46	0.234	86.89°
0.30	0.01209	11.31	0.269	86.28°
0.40	0.01401	11.23	0.295	86.09°
0.50	0.01387	11.57	0.308	85.70°
0.60	0.01310	12.27	0.309	86.54°
0.70	0.01279	13.02	0.308	86.48°
0.80	0.01317	13.32	0.313	86.18°

It is observed that the wave angle of the most amplified stationary disturbances remains almost constant in the chordwise direction. The constant phase lines of the most unstable stationary disturbances are inclined at angles less than five degrees with respect to the inviscid streamline.

Third, we introduce stationary and traveling disturbances separately at x_1/c=0.06 and perform a linear PSE analysis to determine both the most amplified frequency and spanwise wave number. In Figure 4.8,

we show a comparison of the linear PSE computation for the stationary disturbance components with measured data of Deyhle and Bippes [9]. The results are presented for the velocity components in the directions tangential and perpendicular to the inviscid streamline. Both the locally parallel and linear PSE computation capture the essential features of the measured disturbance profiles like the triple-peak structure and the location of the crossflow-component maximum very well. Despite the good qualitative agreement of the computed crossflow component with the experimental results, we note that the magnitudes obtained from measurement and computation differ by a factor of two. This was also reported by Deyhle and Bippes [9] and is attributed to the presence of small spanwise gradients in the mean flow. Further, the local theory is predicting a slightly too high peak location of the tangential component, whereas the linear PSE matches the experimental data better.

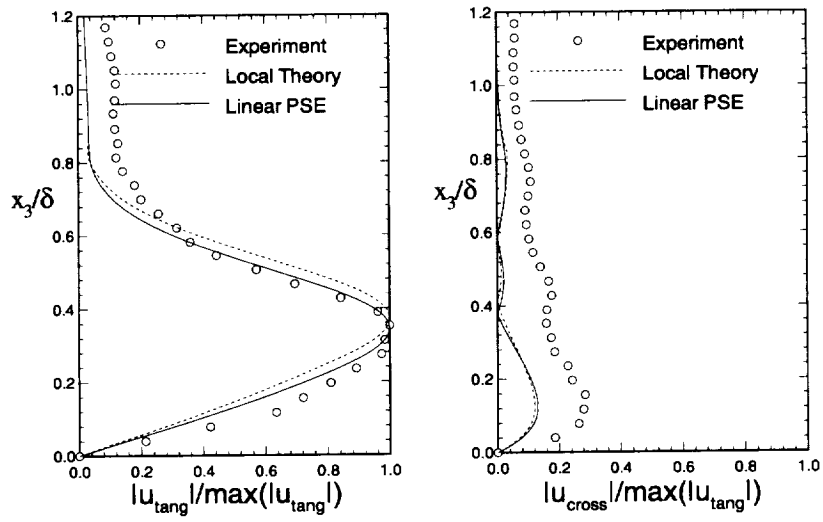

FIG. 4.8. *Stationary disturbance profiles from experiment and computation at* x_1/c=0.6

Finally, Figure 4.9 shows both the calculated linear and nonlinear growth rates based on the u_1-component, as well as the N-factors for the most amplified modes. The obtained values for the most amplified spanwise wavelength $\lambda^*_{z_2}$=12mm, the most amplified frequency f^*=178Hz, and the maximum N-factor of $N\simeq$16 for the traveling disturbance agree exactly with previous work [4]. We also note from Figure 4.9, that the traveling disturbances are much more amplified than the stationary disturbances.

4.3. Nonlinear Analysis. Since our formulation does not include the receptivity to freestream turbulence or surface roughness, we match the initial amplitudes of the disturbances with those given by Bertolotti [4] at x_1/c=0.1. The amplitude is defined as $A = |u_1|_{max}/U_\infty$. For $A_{s,u} = 0.04\%$ in the body-fixed coordinate system, we obtain the same value for the disturbance component along the inviscid streamline $u_{tang,avg} = (u_{tang,max} - u_{tang,min})/2$ at x_1/c=0.1 as shown by Bertolotti. Here, the subscripts *max* and *min* stand for the maximum and minimum value of an average in the spanwise direction. For the nonlinear computations in this section, we include eight modes in spanwise direction and four modes for the frequency. As reported by Bertolotti [4] and in Section 3.2, we find that the purely stationary disturbance saturates at a higher amplitude level and a later streamwise location than in the experiment. Therefore, we include a small amplitude traveling disturbance with the most amplified frequency of f^*=178Hz in the computations ($A_{t,u} = 0.004\%$).

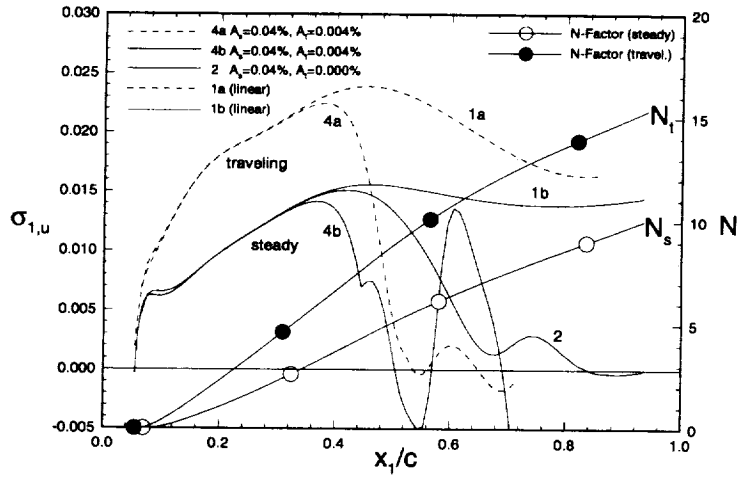

FIG. 4.9. *Linear and nonlinear growth rates and N-Factors for $\lambda^*_{z_2}$ =12mm, f^* =178Hz*

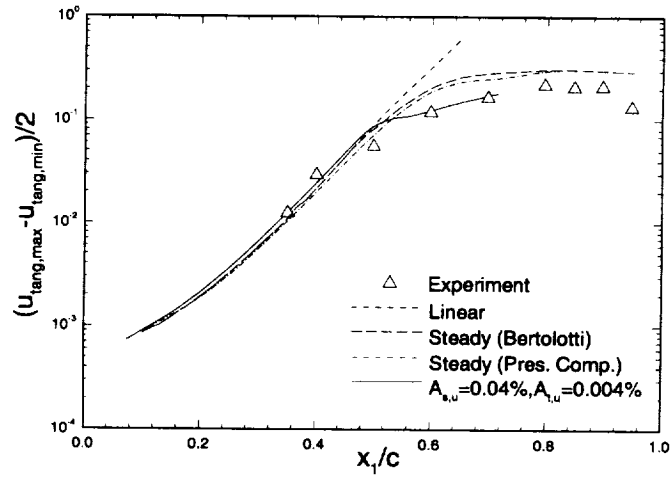

FIG. 4.10. *Amplitude growth from experiment and computation*

In the nonlinear cases, the wave number and frequency domains are modeled using 8×4 modes for β_1 and ω, respectively. Allowing for the nonlinear interaction of these disturbances, the saturation onset is shifted upstream and the saturation amplitude decreases. Figure 4.10 shows the measured and computed evolution of the disturbances along the chord. We observe that the saturation onset is predicted slightly late, but the experimental saturation amplitude is matched quite well.

Next, we describe the spatial development of the crossflow vortices. Figure 4.11 shows the u_1-disturbance component at x_1/c=0.5, 0.6, and 0.7 for both the purely stationary and the interaction case together with the experimental data at x_1/c=0.6. It is seen that the purely stationary vortices from the computation at x_1/c=0.6 are further developed than the measured vortices. Both their extension in the normal direction and their degree of distortion are overpredicted. In the interaction case, however, the normal extension of the vortices has decreased to the experimental value, but the structure of the vortices is more distorted than shown in the experimental results. This difference may be attributed to the longer growth of the

disturbances in the computation that results into an earlier development of the roll-over of positive and negative disturbance components.

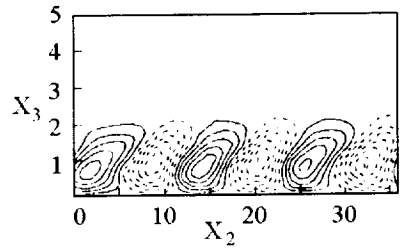

Experimental data at x_1/c=0.60 (Bertolotti, 1996)

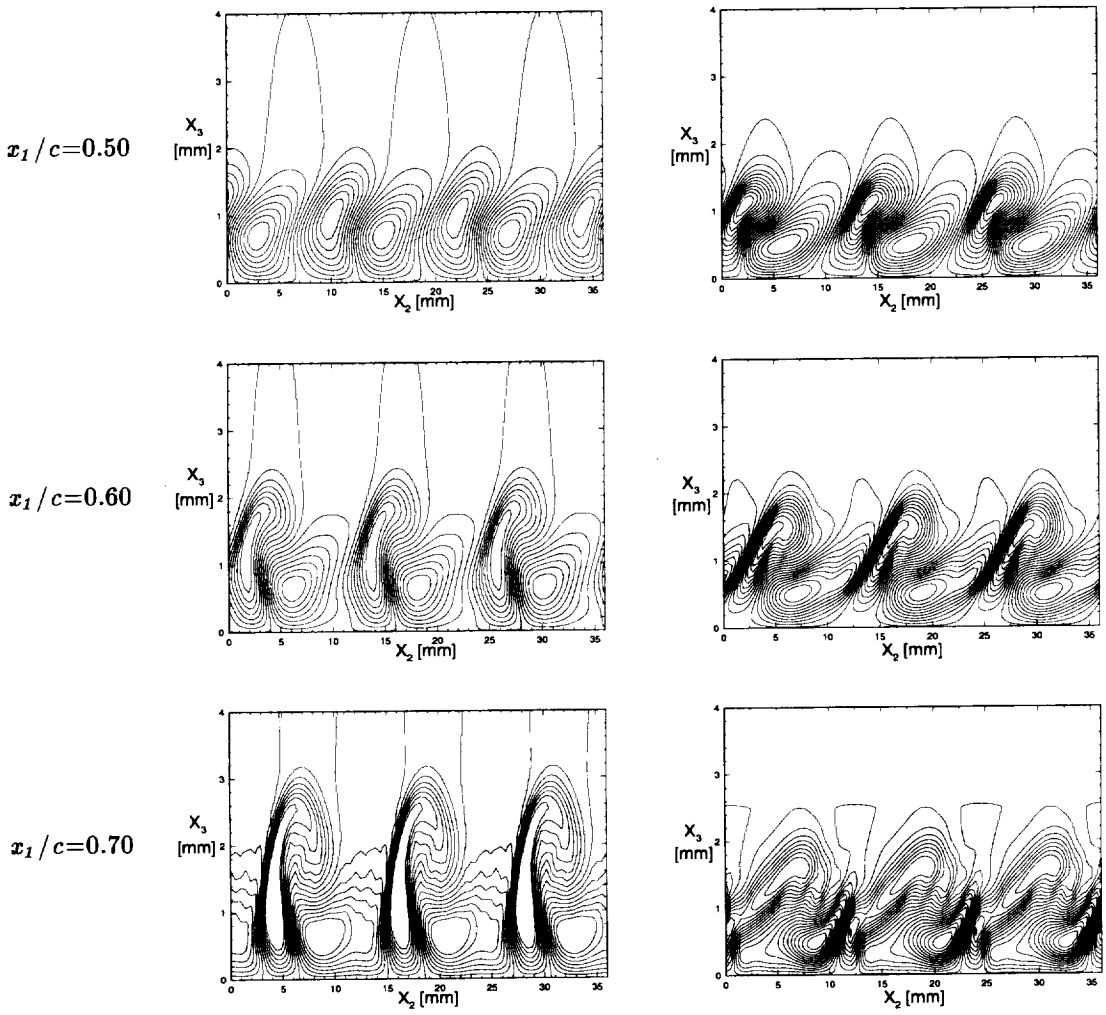

a) Steady Case b) Interaction Case at T=0

FIG. 4.11. *Total u_1-disturbance quantity from a PSE computation*

In order to further describe the purely stationary vortex that will be investigated for its instability to three-dimensional high-frequency secondary disturbances in Part 2 of the paper, we show the shape functions of the individual modes and the total velocity component along the stationary vortex at different spanwise

positions in Figures 4.12 and 4.13, respectively. Here, u_1 and w_1 are the velocity components perpendicular and tangential to the constant phase lines (see Figure 2.1).

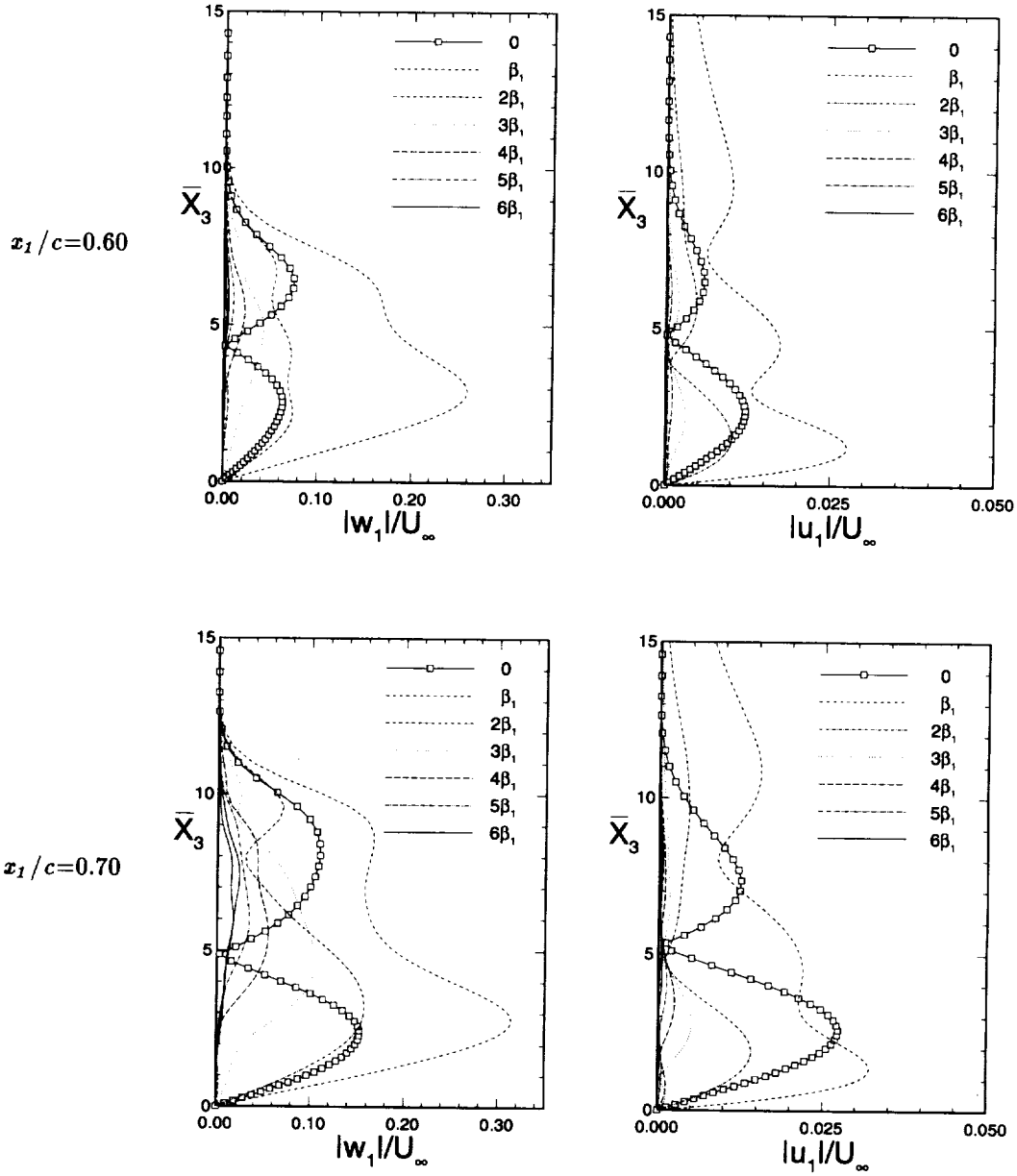

FIG. 4.12. *Shape functions of individual modes at two streamwise locations*

For the two streamwise positions we selected, it can be seen from Figure 4.10 that the stationary disturbances are about to saturate at x_1/c=0.6 where they reach amplitudes of $A_{s,u} \simeq 20\%$. At x_1/c=0.7, they are fully saturated at an amplitude level of $A_{s,u} \simeq 30\%$. As observed for Swept Hiemenz Flow in Section 3.2., Figure 4.13 reveals the presence of highly inflectional profiles at both streamwise locations. Comparing the results presented in Figure 4.12 with the shape functions for Swept Hiemenz Flow in Figure 3.4, we note the very similar shape and even magnitude of the individual shape functions in this region of nonlinear saturation of the stationary crossflow vortex.

x_1/c=0.60

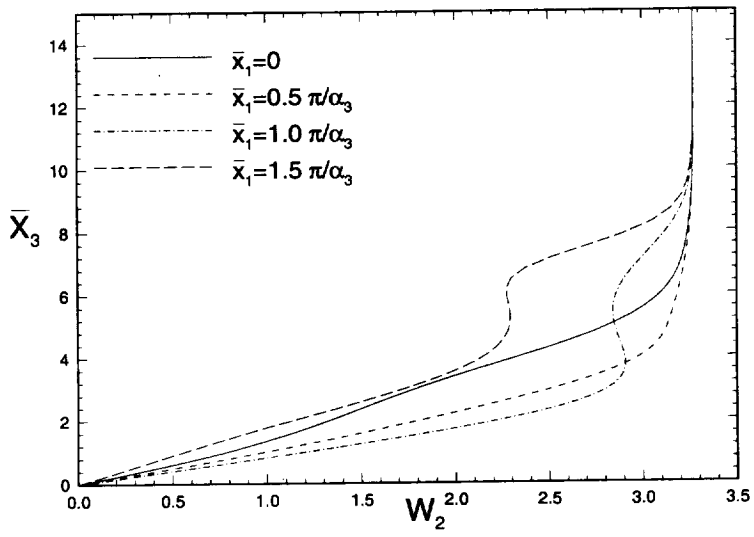

x_1/c=0.70

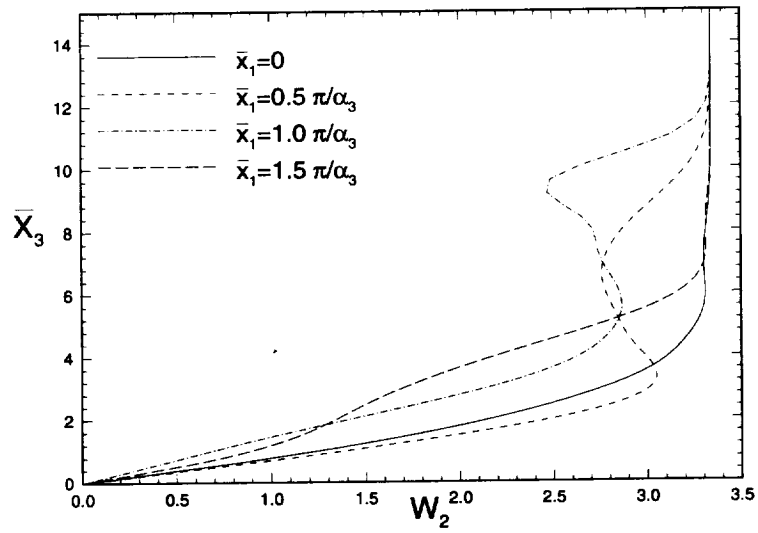

FIG. 4.13. *Total flow quantity along the stationary vortex for different spanwise stations*

Summarizing the previous plots and visualizing the spatial development of the flow in the region of nonlinear saturation, we plot the development of the crossflow vortices for both the purely stationary and the interaction case in Figures 4.14 and 4.15. Shown are the contours of the total velocity component in the chordwise direction in the region between 50% and 70% chord length, where the nonlinear interaction of the disturbance components dominates the physics of the flow. Clearly observed are the developing distortion of the boundary layer at x_1/c=0.50, and the roll-up of the vortices in the positive spanwise direction in the purely stationary case. For the interaction case at time T=0, we first note that the disturbances do not reach as far into the outer flow and the lift-up of low-speed fluid away from the wall is not as strong as in the stationary case. Second, we see a strong vortex core away from the wall at a location where the stationary vortex rolls over.

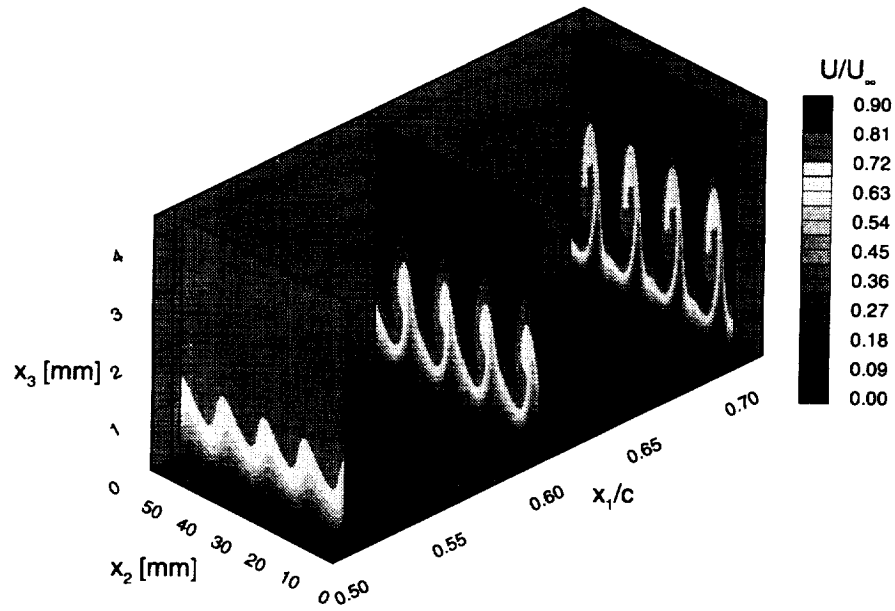

FIG. 4.14. *Evolution of crossflow vortices : Stationary vortex*

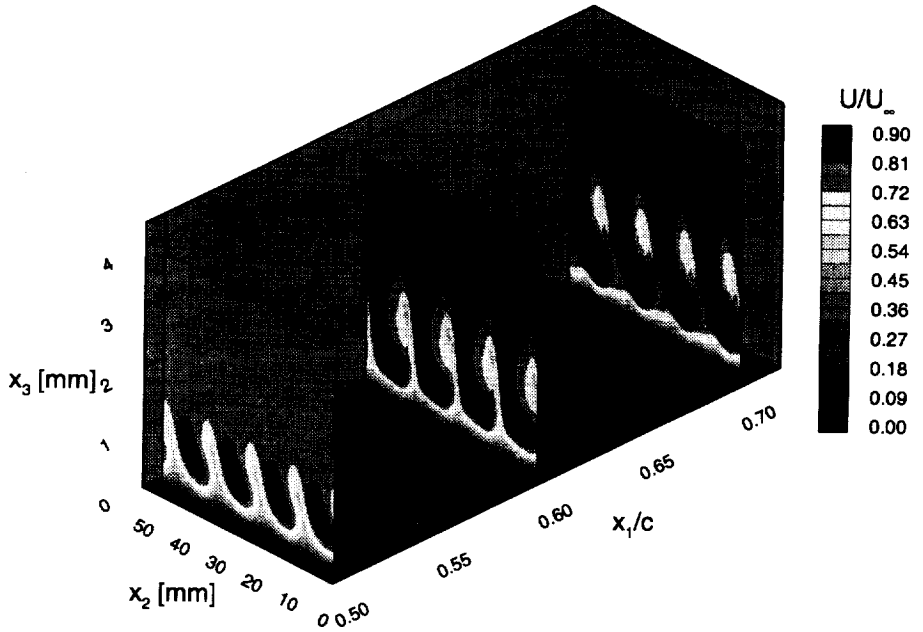

FIG. 4.15. *Evolution of crossflow vortices : Interaction case at T=0*

5. Conclusion. In the present paper, we studied the linear and nonlinear stability of crossflow dominated three-dimensional boundary layers using the PSE. We investigated Swept Hiemenz Flow and the DLR Transition Experiment. We described the structure of the stationary vortex in the region of nonlinear saturation in detail. Investigating the DLR Experiment, we computed the mean flow directly from the measured pressure distribution. The linear results for wave angle, wavelength and phase velocity obtained by spatial

theory agree reasonably well with the experimental results. Better agreement was found for the disturbance eigenfunctions. From our nonlinear computations, we could confirm that including a small amplitude traveling mode in the analysis decreases the saturation amplitude of the physical velocity component significantly, and our results match the spanwise averaged experimental data well. For both investigated problems, we documented the existence of strongly inflectional profiles along the direction of the statio nary vortex in the region of nonlinear saturation. It seems that a very strong fundamental mode and a large mean flow distortion are the key-players in setting up the flow for a high-frequency secondary instability that will be investigated in Part 2 of this paper.

REFERENCES

[1] D. ARNAL AND J.C. JUILLEN, *Three-dimensional transition studies at ONERA/CERT*, AIAA Paper 87-1335, 1987.

[2] P. BALAKUMAR AND M.R. MALIK, *Waves produced from a harmonic point source in a supersonic boundary layer flow*, Journal of Fluid Mechanics **245** (1992), pp. 229–247.

[3] F.P. BERTOLOTTI, T. HERBERT, AND P. SPALART, *Linear and nonlinear stability of the Blasius boundary*, Journal of Fluid Mechanics **242** (1992), pp. 441–474.

[4] F.P. BERTOLOTTI, *On the birth and evolution of disturbances in three-dimensional boundary layers*, IUTAM Symposium on Nonlinear Instability and Transition in 3D Boundary Layers, Kluwer Academic Publishers, the Netherlands, 1996, pp. 247–256.

[5] F.P. BERTOLOTTI, personal communication.

[6] C.-L. CHANG, M.R. MALIK, G. ERLEBACHER, AND M.Y. HUSSAINI, *Compressible stability of growing boundary layers using Parabolized Stability Equations*, AIAA Paper 91-1636, 1991.

[7] K. CHAPMAN, M.S. REIBERT, W.S. SARIC, AND M. GLAUSER, *Boundary layer transition detection and structure identification through surface shear stress measurements*, AIAA Paper 98-0782, 1998.

[8] H. DEYHLE, G. HOEHLER, AND H. BIPPES, *Experimental investigation of instability wave propagation in a three-dimensional boundary layer flow*, AIAA Journal **31**, No. 4, (1993), pp. 637–645.

[9] H. DEYHLE AND H. BIPPES, *Disturbance growth in an unstable three-dimensional boundary layer and its dependence on environmental conditions*, Journal of Fluid Mechanics **316** (1992), pp. 73–113.

[10] TH. HERBERT AND F.P. BERTOLOTTI, *Stability analysis of non-parallel boundary layers*, Bulletin of the American Physical Society **32** (1987), p. 2079.

[11] TH. HERBERT AND M.V. MORKOVIN, *Dialog on bridging some gaps in stability and transition research*, Laminar-Turbulent Transition, Springer, 1980, pp. 47–72.

[12] TH. HERBERT, *Boundary layer transition — analysis and prediction revisited*, AIAA Paper 91-0737, 1991.

[13] R.D. JOSLIN AND C.L. STREETT, *The role of stationary crossflow vortices in boundary layer transition*, Physics of Fluids **6** (1994), pp. 3442-3453.

[14] Y. KOHAMA, W.S. SARIC, AND J. HOOS, *A high-frequency secondary instability of crossflow vortices that leads to transition*, Proc. R.A.S. Boundary Layer Transition and Control, Cambridge, U.K., 1991.

[15] L.M. MACK, *3D-Effects in boundary layer stability*, in 12^{th} Symposium on Naval Hydrodynamics, 1978.

[16] M.R. MALIK, S. CHUANG, AND M.Y HUSSAINI, *Accurate numerical solution of compressible, linear stability equations*, Zeitschrift für Angewandte Mathematik und Physik **33**, No. 2, (1982), pp. 189–201.

[17] M.R. MALIK, F. LI, AND C.-L. CHANG, *Crossflow disturbances in three-dimensional boundary layers: Nonlinear development, wave interaction and secondary instability*, Journal of Fluid Mechanics **268**(1994), pp. 1–36.

[18] M.S. REIBERT, W.S. SARIC, AND R.B. CARILLO, *Experiments in nonlinear saturation of stationary crossflow vortices in a swept wing boundary layer*, AIAA Paper 96-0184, 1996.

[19] W.S. SARIC, R.B. CARILLO, AND M.S. REIBERT, *Leading Edge roughness as a transition control mechanism*, AIAA Paper 98-0781, 1998.

REPORT DOCUMENTATION PAGE

Form Approved
OMB No. 0704-0188

Public reporting burden for this collection of information is estimated to average 1 hour per response, including the time for reviewing instructions, searching existing data sources, gathering and maintaining the data needed, and completing and reviewing the collection of information. Send comments regarding this burden estimate or any other aspect of this collection of information, including suggestions for reducing this burden, to Washington Headquarters Services, Directorate for Information Operations and Reports, 1215 Jefferson Davis Highway, Suite 1204, Arlington, VA 22202-4302, and to the Office of Management and Budget, Paperwork Reduction Project (0704-0188), Washington, DC 20503.

1. AGENCY USE ONLY *(Leave blank)*

2. REPORT DATE
May 1999

3. REPORT TYPE AND DATES COVERED
Contractor Report

4. TITLE AND SUBTITLE
On the stability of three-dimensional boundary layers
Part 1: Linear and nonlinear stability

5. FUNDING NUMBERS
C NAS1-97046
WU 505-90-52-01

6. AUTHOR(S)
Erik Janke
Ponnampalam Balakumar

7. PERFORMING ORGANIZATION NAME(S) AND ADDRESS(ES)
Institute for Computer Applications in Science and Engineering
Mail Stop 132C, NASA Langley Research Center
Hampton, VA 23681-2199

8. PERFORMING ORGANIZATION REPORT NUMBER
ICASE Report No. 99-16

9. SPONSORING/MONITORING AGENCY NAME(S) AND ADDRESS(ES)
National Aeronautics and Space Administration
Langley Research Center
Hampton, VA 23681-2199

10. SPONSORING/MONITORING AGENCY REPORT NUMBER
NASA/CR-1999-209330
ICASE Report No. 99-16

11. SUPPLEMENTARY NOTES
Langley Technical Monitor: Dennis M. Bushnell
Final Report
Submitted to Theoretical and Computational Fluid Dynamics

12a. DISTRIBUTION/AVAILABILITY STATEMENT
Unclassified Unlimited
Subject Category 34
Distribution: Nonstandard
Availability: NASA-CASI (301) 621-0390

12b. DISTRIBUTION CODE

13. ABSTRACT *(Maximum 200 words)*
The primary stability of incompressible three-dimensional boundary layers is investigated using the Parabolized Stability Equations (PSE). We compute the evolution of stationary and traveling disturbances in the linear and nonlinear region prior to transition. As model problems, we choose Swept Hiemenz Flow and the DLR Transition Experiment. The primary stability results for Swept Hiemenz Flow agree very well with computations by Malik et al. For the DLR Experiment, the mean flow profiles are obtained by solving the boundary layer equations for the measured pressure distribution. Both linear and nonlinear results show very good agreement with the experiment.

14. SUBJECT TERMS
PSE, crossflow instability, 3D boundary layers

15. NUMBER OF PAGES
25

16. PRICE CODE
A03

17. SECURITY CLASSIFICATION OF REPORT	18. SECURITY CLASSIFICATION OF THIS PAGE	19. SECURITY CLASSIFICATION OF ABSTRACT	20. LIMITATION OF ABSTRACT
Unclassified	Unclassified		